

Teleseismic body waveforms and receiver structures beneath seismic stations

Lian-She Zhao and Cliff Frohlich

Institute for Geophysics, The University of Texas at Austin, 8701 N. MoPac Expressway, Austin, TX 78759-8397

Accepted 1995 September 1. Received 1995 July 25; in original form 1995 February 12

SUMMARY

In this paper we describe a practical method for determining crustal structure by comparing observations of teleseismic body waves with synthetics constructed using generalized ray theory. Layered crustal structure beneath a seismic station strongly influences teleseismic body waves arriving in the 50 s or so after the initial *P*; however, the effect of crustal structure differs significantly for vertical-component and radial-component records. For any proposed crustal structure, we develop an approximate theoretical formulation to predict the radial-component seismogram as a function of the vertical-component observations. Then, we compare the observed and predicted radial-component seismograms in the time domain, and vary the proposed crustal structure using a grid-search scheme until we obtain an optimum match. The theoretical approximation is complete to second order in the reflection and transmission coefficients, and is accurate to within a few per cent for modelling teleseismic waveforms. We demonstrate the feasibility of this second-order, radial-vertical comparison (SORVEC) method by testing it on synthetically generated waveforms having complicated source properties and significant levels of background noise. We illustrate the application to real data by determining the crustal structure beneath two seismic stations in Tibet, LZH and AMDO. Beneath station LZH, the crustal thickness is about 65 km. Beneath station AMDO, the crustal thickness is about 75 km, and there is a low-velocity layer in the lower crust.

Key words: body waves, crustal structure, *P* waves, seismic velocities, seismology.

INTRODUCTION

For a long time seismologists have known that analysis of the crustal effects on teleseismic *P* waveforms might provide an effective way to determine crustal and uppermost-mantle velocity structure. Phinney (1964) used a Haskell matrix approach to model the so-called 'transfer function' $T(\omega) = |Z(\omega)|/|H(\omega)|$, where $Z(\omega)$ and $H(\omega)$ are amplitude spectra of the vertical and horizontal components. Subsequently, numerous investigators used spectral ratios to study crustal structure (see Báth 1974 for a review). Langston (1979) utilized the inverted transfer function H/Z in the time domain; subsequently, people have called this the 'receiver function' (Owens, Zandt & Taylor 1984). More recently, numerous researchers have applied receiver function methods to study near-receiver velocity structure and to evaluate model-parameter sensitivity (e.g. Owens *et al.* 1984; Ammon, Randall & Zandt 1990; Cassidy 1992; Mangino & Ebel 1992). Langston (1989) and Owens, Crosson & Hendrickson (1988) noticed that dipping structures beneath

seismic stations have significant effects on receiver functions. Gurrola & Minster (1993) have applied receiver functions to study discontinuities in the upper mantle.

A practical difficulty with nearly all of the transfer/receiver function methods occurs because of the division by either the vertical- or radial-component signal; significant distortions may occur if there are zeros in the signal or noise spectrum. Moreover, the use of a linearized inversion scheme to solve this highly non-linear problem (Ammon *et al.* 1990) may produce velocity models which are strongly dependent on the initial starting models. Another approach to this problem is to model both vertical and radial components in the time domain (Burdick & Langston 1977). While this incorporates the physics of near-station crustal effects more clearly, the difficulty is that the source-time function is an unknown factor. Burdick & Langston (1977) avoided this problem somewhat by evaluating signals from deep earthquakes. Nevertheless, in spite of all these efforts, there is no unanimity about the best way to evaluate the effects of crustal layering on teleseismic waveforms. For shallow earthquakes, the waveform

complications caused by the crust have not gained much attention.

In this paper we propose a new approach for determining near-station velocity structure, which we call the second-order radial/vertical comparison (SORVEC) method. The SORVEC method avoids many of the problems with, and combines desirable features from, both approaches described above. Unlike Burdick & Langston (1977), we do not model vertical-component signals in the time domain, but instead use the vertical-component seismograms as an input signal for an inversion, because they closely resemble the signal leaving the source region. Unlike Langston (1979), our approach completely avoids making any explicit assumptions about the spectral properties of the source signal, the noise, or about the source-time functions. A theoretical analysis demonstrates that our approach is exact to the second order in the reflection/transmission coefficients. Thus, it provides reasonable results when applied to teleseismic waveforms which arrive at the base of the crust with near-vertical angles of incidence.

In practical terms, recovering crustal structure from teleseismic observations is complicated because receiver functions become very complex, even when the earthquake source is a delta function and the crustal structure is a simple layer over a half-space (Fig. 1). In ray-theoretical terms, the arriving signal contains numerous reverberations, due to crustal layering both near the source (Fig. 2) and near the receiver (Fig. 3). What makes it possible to recover crustal structure is the fact that the relative amplitudes of particular reverberations are different for vertical-component and radial-component signals. Fortunately, even when crustal structure is complex, at teleseismic distances a comparison of synthetics generated with a full reflectivity (Fuchs & Müller 1976) and with generalized ray theory (Helmberger 1980) reveals that only a relatively few rays contribute significant energy to the arriving signal (Fig. 4). For example, with one layer (Fig. 3), seven rays are adequate, whereas nine are required when there are two layers (Fig. 4). The fact that only a few rays are significant makes grid-search methods for determining crustal structure possible and practical, because one need only evaluate a relatively few transmission and reflection coefficients for each candidate model—our approach is approximately 1000 times faster than a full Haskell matrix calculation. We will return to this point later.

Thus, in the present study we shall first develop the theoretical background for the SORVEC method, then use synthetic seismograms determined with generalized ray theory to demonstrate its feasibility as a practical scheme for recovering near-station crustal structure. Then, we apply the method to synthetic waveforms to test its performance, and finally, to demonstrate its practical use, we apply the method to seismograms recorded at two stations in Tibet.

THEORY OF THE SORVEC METHOD

Suppose that the P signal arriving at the base of the crust from a teleseismic event is $S(t)$, which includes both the source signal and complexity caused by near-source structure (Fig. 2). Then, the observed vertical-component seismogram $Z(t)$ and radial-component seismogram $H(t)$ are

$$Z(t) = z_0 S(t) + \sum_i z_i S(t - t_i), \quad (1)$$

and

$$H(t) = r_0 S(t) + \sum_i r_i S(t - t_i), \quad (2)$$

where z_i and r_i are the appropriate products of receiver responses and transmission and reflection coefficients from the Moho to the free surface along the ray path. The t_i are the time delays for reflected and converted rays in the crust.

We normalize both the vertical component $Z(t)$ and the radial component $H(t)$ to unit maximum amplitudes and rewrite eqs (1) and (2) as

$$Z(t) = S(t) \left[1 + \sum_i \frac{z_i}{z_0} \delta(t - t_i) \right] \quad (3)$$

and

$$H(t) = S(t) \left[1 + \sum_i \frac{r_i}{r_0} \delta(t - t_i) \right]. \quad (4)$$

We then Fourier transform eqs (3) and (4), writing $\hat{\delta}_i(\omega)$ as the transform of $\delta(t - t_i)$, and expand to second order in z_i and r_i to obtain

$$Z(\omega) = S(\omega) \left[1 + \sum_i \frac{z_i}{z_0} \hat{\delta}_i(\omega) \right] \quad (5)$$

and

$$H(\omega) = S(\omega) \left[1 + \sum_i \frac{r_i}{r_0} \hat{\delta}_i(\omega) \right] = \frac{Z(\omega) \left[1 + \sum_i \frac{r_i}{r_0} \hat{\delta}_i(\omega) \right]}{1 + \sum_i \frac{z_i}{z_0} \hat{\delta}_i(\omega)} \quad (6)$$

$$\cong Z(\omega) \left[1 + \sum_i \frac{r_i}{r_0} \hat{\delta}_i(\omega) \right] \quad (0\text{th order}),$$

$$\cong Z(\omega) \left[1 + \sum_i \left(\frac{r_i}{r_0} - \frac{z_i}{z_0} \right) \hat{\delta}_i(\omega) \right] \quad (1\text{st order}),$$

$$\cong Z(\omega) \left\{ 1 + \sum_i \left(\frac{r_i}{r_0} - \frac{z_i}{z_0} \right) \hat{\delta}_i(\omega) \times \left[1 - \sum_j \frac{z_j}{z_0} \hat{\delta}_{t_j}(\omega) \right] \right\} \quad (2\text{nd order}),$$

$$\cong Z(\omega) \left[1 + \sum_i \left(\frac{r_i}{r_0} - \frac{z_i}{z_0} \right) \hat{\delta}_i(\omega) \times \left\{ 1 - \sum_j \frac{z_j}{z_0} \hat{\delta}_{t_j}(\omega) + \dots + \left[- \sum_j \frac{z_j}{z_0} \hat{\delta}_{t_j}(\omega) \right]^{n-1} \right\} \right] \quad (n\text{th order}).$$

In the time domain, these expressions for the normalized radial component are

$$H(t) \cong Z(t) + \sum_i \frac{r_i}{r_0} Z(t - t_i) \quad (0\text{th order}),$$

$$\cong Z(t) + \sum_i \left(\frac{r_i}{r_0} - \frac{z_i}{z_0} \right) Z(t - t_i) \quad (1\text{st order}),$$

$$\cong Z(t) + \sum_i \left(\frac{r_i}{r_0} - \frac{z_i}{z_0} \right) [Z(t - t_i) - Y_2(t - t_i)] \quad (2\text{nd order}),$$

$$\cong Z(t) + \sum_i \left(\frac{r_i}{r_0} - \frac{z_i}{z_0} \right) [Z(t - t_i) - Y_2(t - t_i) - \dots - Y_n(t - t_i)], \quad (n\text{th order}). \quad (7)$$

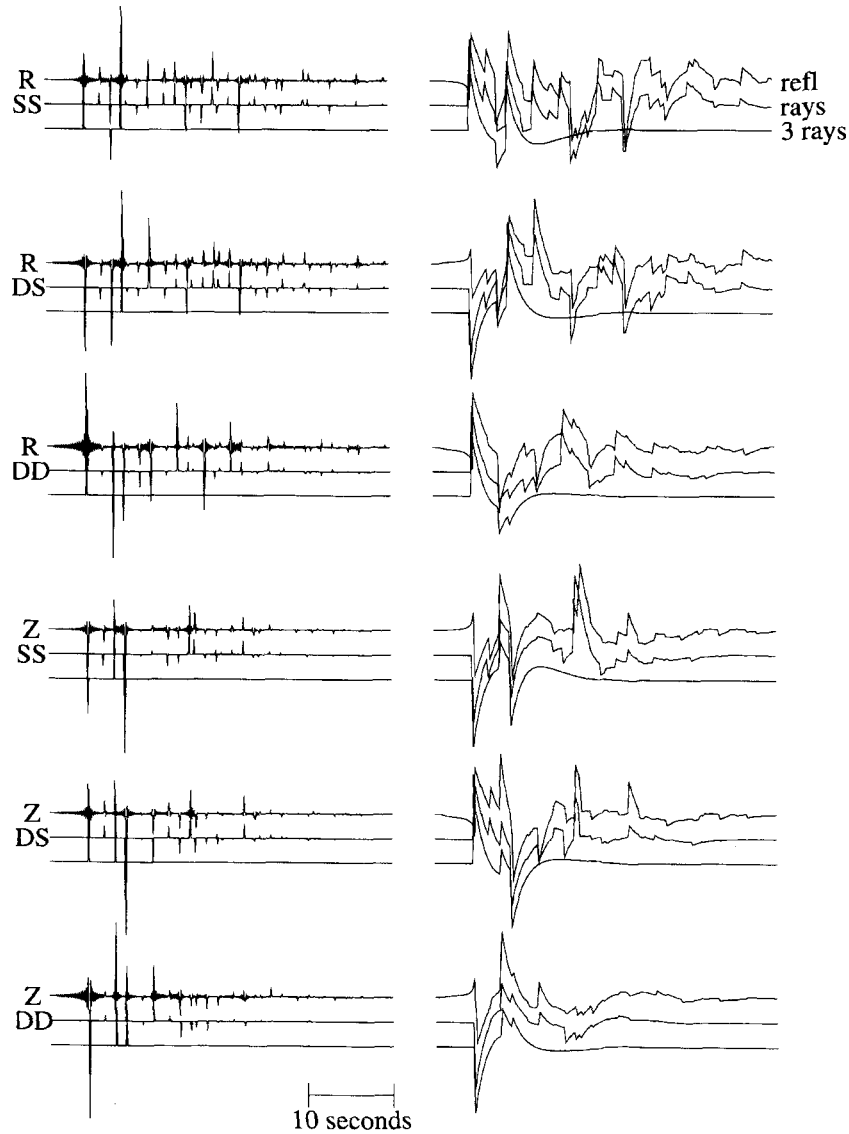


Figure 1. Synthetics of radial-component (top three traces) and vertical-component (bottom three traces) teleseismic body waveforms are extremely complex and depend strongly on the type of source, even when they are generated using very simple crustal models and an impulsive source-time function. On the left-hand side are broad-band synthetics, including frequencies up to 4 Hz; these are filtered on the right-hand side with the long-period WWSSN instrument response. In each group of three traces, the top trace is calculated using reflectivity (Fuchs & Müller 1976), and the bottom two traces are calculated using generalized ray theory; however, the bottom trace includes only the rays P , pP and sP . Here, the source depth is 10 km, the source–receiver distance is 70° , and both the source and receiver regions possess a layer-over-a-half-space crustal model adapted from PREM (Dziewonski & Anderson 1980): a one-layer crust with a P velocity of 6.2 km s^{-1} , an S velocity of 3.5 km s^{-1} , and a thickness of 24.4 km, overlying a half-space mantle with a P velocity of 8.11 km s^{-1} and S velocity of 4.49 km s^{-1} . ‘SS’, ‘DS’ and ‘DD’ are the synthetics for source mechanisms of strike-slip, dip-slip, and 45° dip-slip, respectively. In each case, the station is assumed to be at an azimuth of 45°E of N; for the ‘SS’ mechanism one nodal plane trends NS; for the dip-slip and 45° dip-slip mechanism the B axis trends NS.

where

$$Y_2 = \sum_i \frac{z_i}{z_0} Z(t - t_i),$$

$$Y_n(t) = - \sum_i \frac{z_i}{z_0} Y_{n-1}(t - t_i).$$

The zero-order approximation is simply eq. (2) with normalized amplitude and $Z(t)$ instead of $S(t)$. In the first-order expression, it is clear that converted and reflected rays arriving at the receiver as a P phase do not contribute to the response. However, in the second-order expression, P arrivals do have

an effect expressed in the $Y(t)$ term, although their contribution is smaller than that of the S arrivals. From the n th-order expression, we can see that each successive term in the expression is multiplied by a factor of z_i/z_0 , which is always less than 0.2–0.3, which occurs for the P -to- S conversion at the Moho. Because eq. (7) is a second-order comparison of the radial-component and vertical-component signals, we call the application of eq. (7) the SORVEC method.

To illustrate the effect of each term in the expansion (eq. 7), we calculate synthetic signals constructed for a layer-over-half-space model (Fig. 5). While the difference between the exact calculation (the ‘real’ trace) and the ‘0th order’ trace is as much

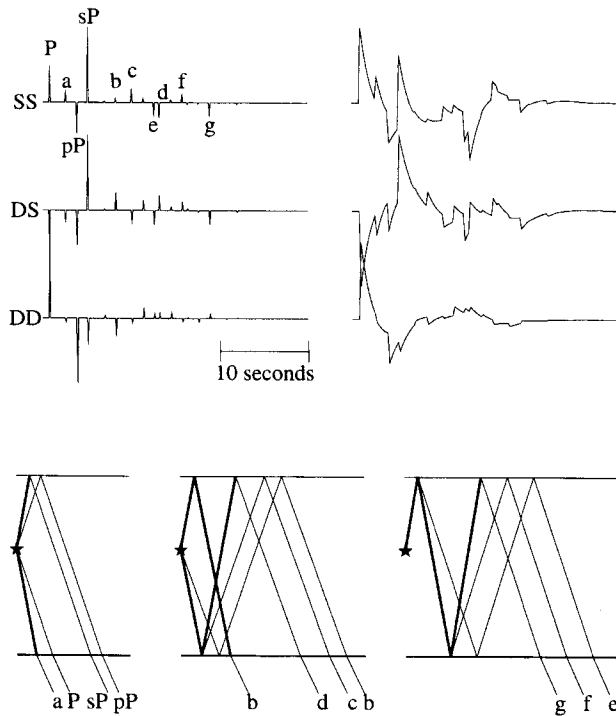


Figure 2. The signal leaving the source region generated from an impulsive source, including both direct rays and reverberations within the crust. The synthetics are broad-band (top left) and long-period (top right) waveforms, with arrivals labelled corresponding to particular ray paths (bottom). The source depth, velocity model, etc. used are the same as in Fig. 1. Thicker lines represent S_v segments; thinner lines are P segments.

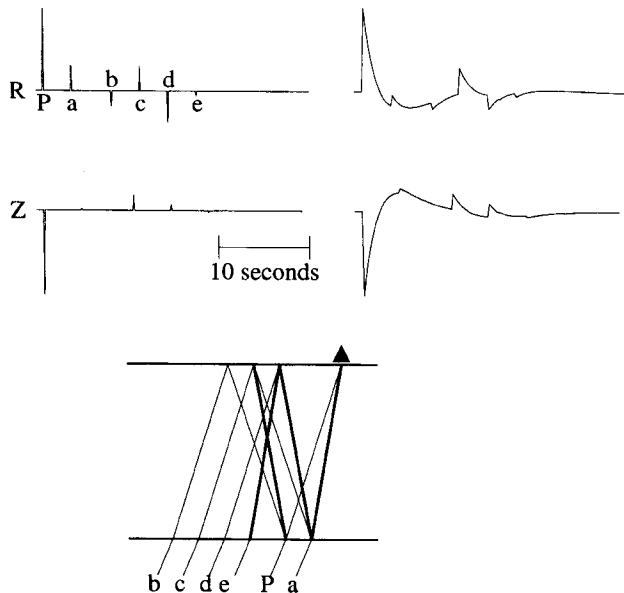


Figure 3. The radial-component (top) and vertical-component (centre) signal arriving at a receiver, generated by a deep, impulsive source, situated well beneath the crust, so that it contains no near-source crustal reverberations; on the left and the right are broad-band and long-period waveforms, respectively. We include only the signal contributions from the seven most important rays (bottom). The contribution of ray 'b' to the receiver function is of second order.

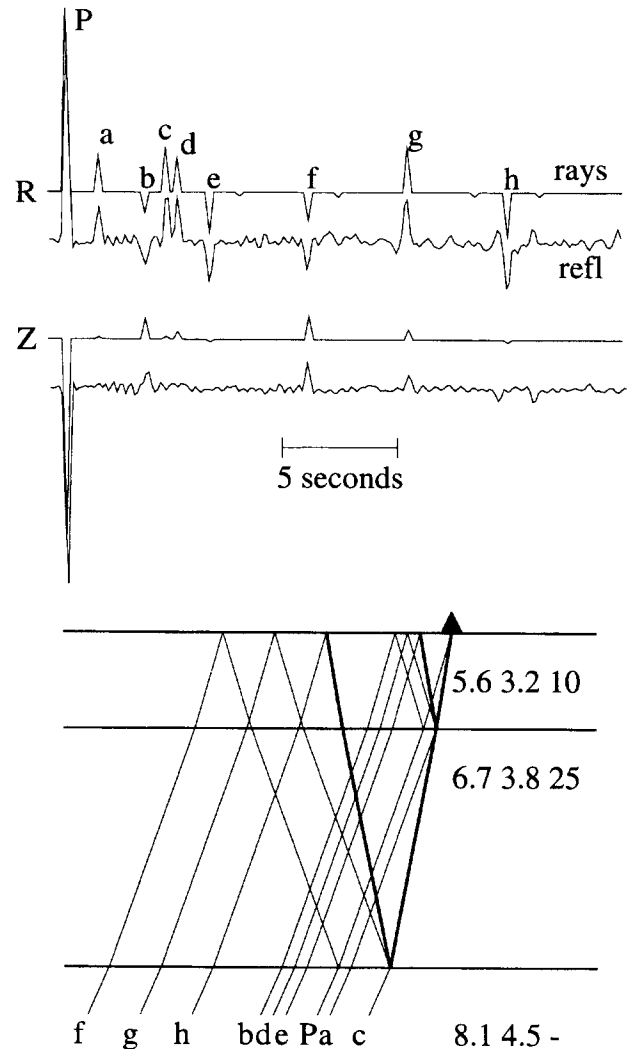


Figure 4. Comparison of radial- (top two traces, labelled R) and vertical-component (middle two traces, labelled Z) synthetics generated using generalized ray theory (upper trace in each pair) and with reflectivity (lower trace) for a two-layer-over-a-half-space model (bottom, numbers at right represent model P and S velocities and layer thicknesses respectively). Only the nine rays with the labelled ray paths have significant energy.

as 15.8 per cent of the maximum trace amplitude, this difference is reduced to only 1.5 per cent when we use the second-order approximation. For all the applications in this paper, we use the second-order approximation; at teleseismic distances this introduces an error in the amplitude that is no more than a few per cent (Fig. 5).

If we trace rays properly, eq. (7) is applicable for 2- and 3-D structures, as well as for 1-D models. For an arbitrarily oriented plane interface, if γ_i is the normal to i th plane, ζ_i is the incident vector to the i th plane, and ζ_{i+1} is the reflection/transmission vector, then all three vectors lie in one plane, have unit length, and satisfy Snell's law. It can be shown that

$$\frac{\zeta_{i+1}}{v_{i+1}} - \frac{\zeta_i}{v_i} = \left[\left(\frac{\zeta_{i+1}}{v_{i+1}} - \frac{\zeta_i}{v_i} \right) \cdot \gamma_i \right] \gamma_i, \quad (8)$$

where v_i is the velocity of the i th layer, and $\zeta_{i+1} \cdot \gamma_i$ is determined by Snell's law. If we begin with ζ_1 , the direction

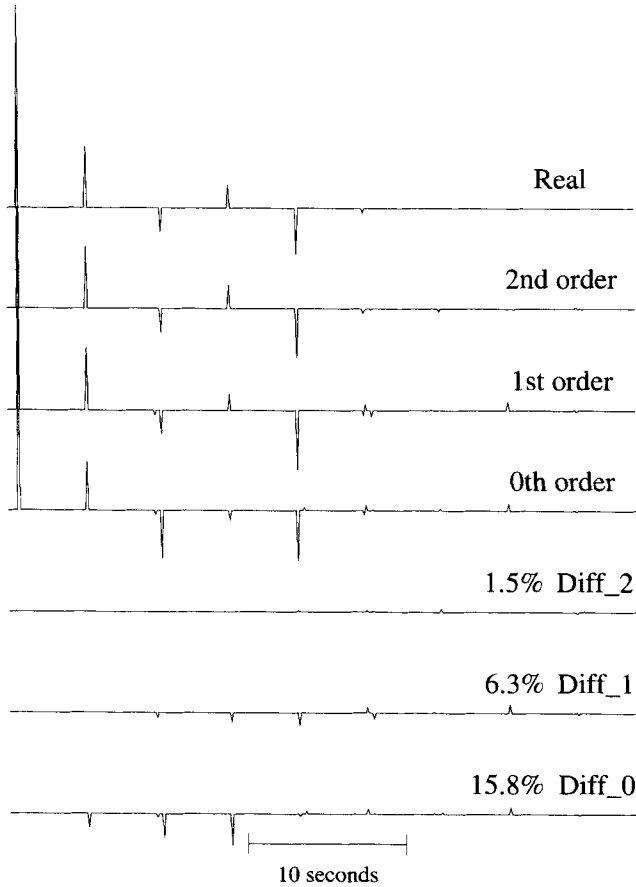


Figure 5. Error introduced from approximations of different order. 'Real' is the synthetic radial component (eq. 2) for a simple layer-over-half-space model (crust: P , S velocities 6.2 km s^{-1} , 3.5 km s^{-1} ; density 2.7 g cm^{-3} ; thickness 32 km ; mantle: 8.2 km s^{-1} , 4.5 km s^{-1} , 3.3 g cm^{-3}). 'Real' is determined using 10 rays: the direct P ray and all P or S reflected or converted rays that bounce once at the Moho. The traces marked 'Diff_{*i*}' are the difference between the 'Real' trace and those determined using the approximate expansion up to order i (eq. 7). The numbers on the left of 'Diff_{*i*}' are the maximum amplitude expressed as a percentage of the maximum amplitude of the 'Real' trace. Synthetics are determined for a source at a distance of 70° . Note that in this example the difference between the real and second order signal is only 1.5 per cent.

vector for the P wave incident at the base of the receiver structure, and determine all the ζ_i ($i = 2, n$), then it is easy to determine the crossing point, \mathbf{R}_i , of the ray and the i th plane:

$$\mathbf{R}_i = \frac{(\mathbf{R}_{i+1} - \mathbf{R}_{i0}) \cdot \boldsymbol{\gamma}_i}{\zeta_{i+1} \cdot \boldsymbol{\gamma}_i} \zeta_{i+1} - \mathbf{R}_{i+1}, \quad (9)$$

where \mathbf{R}_{i0} is any point on the i th plane and, since the last point, \mathbf{R}_n , is the receiver, we use it as the origin. From eqs (8) and (9), we can determine the traveltime of a given ray easily. Langston (1977) used coordinate transform methods and produced formulas which correspond to eqs (8) and (9), but which are somewhat more complicated.

PRACTICAL DETAILS OF THE SORVEC METHOD

The software implementing the SORVEC method is a FORTRAN program which evaluates vertical- and radial-

component teleseismic waveforms from one or more earthquakes to determine the best-fitting 1-D velocity structure with up to five layers beneath a recording station. For each trial crustal structure and vertical-component signal, the program compares the observed radial-component signal with the radial-component signal calculated from eq. (7), utilizing explicit formulas from Helmberger (1968, 1980) for the time delays, t_i , and the reflection and transmission coefficients, r_i and z_i .

The program selects the preferred crustal structure as the one for which the fit between the observed and calculated radial-component signals has the smallest error. The error definition used for fitting is a combination of the L1 and L2 norms,

$$e = \frac{1}{n} \sum_{i=1}^n \Omega_i (e_{1i} + \sqrt{e_{2i}}). \quad (10)$$

Here Ω_i is the weight for the i th record, and e_{1i} and e_{2i} are the errors for the L1 and L2 norms, given by:

$$e_1 = \int |f_{\text{obs}}(t) - f_{\text{syn}}(t)| dt,$$

$$e_2 = \int [f_{\text{obs}}(t) - f_{\text{syn}}(t)]^2 dt,$$

where f_{obs} is the observed radial component, and f_{syn} is the synthetic radial component for a given velocity model.

In the SORVEC approach we normalize both the vertical- and radial-component seismograms. Theoretically, it would help to use absolute amplitude information, as suggested by Ammon (1991) and praised by Cassidy (1992); this is certainly true when the initial amplitude of the radial-component signal is that of the direct P wave, since then the shear velocity, β , of the surface layer can be determined easily from the ratio, χ , of radial-component to vertical-component amplitudes,

$$\beta = \frac{1}{\sqrt{2}} \frac{\chi}{p} \sqrt{\frac{1}{1 + \chi^2 + \sqrt{1 + \chi^2}}}, \quad (11)$$

where p is the ray parameter. This equation is easily derivable from Helmberger's (1968) formulas of vertical and radial receiver functions. Note that Helmberger's receiver function is the site response, which is different from the receiver function used later for Langston's method (1979). However, in practice we find that absolute amplitude information is not useful because for nearly all realistic crustal structures there is interference between the P wave and P - S_v converted phases within the uppermost crustal layer: these exert a strong influence on absolute amplitudes of the radial-component signal. Since the time delay between the two arrivals is generally very small, in practice it is very difficult to separate them unless the uppermost layer is unrealistically thick [e.g. Cassidy (1992) assumed a 20 km thick layer with a shear velocity of 2.89 km s^{-1}]. If the uppermost layer is 5 km thick, there is only 0.8 s separation between the initial P arrival and the P - S_v converted phase, PS_1 (Fig. 6) from the uppermost layer; hence, if the instrumentation can only resolve signals in the period range 1 – 4 s , the initial amplitude of the radial-component signal is not that of the P wave. Thus, if we cannot distinguish the two phases, then the measured value of χ will not represent the amplitude ratio for the direct P phase, and, from eq. (11), we will find a too large surface layer velocity, β . For example,

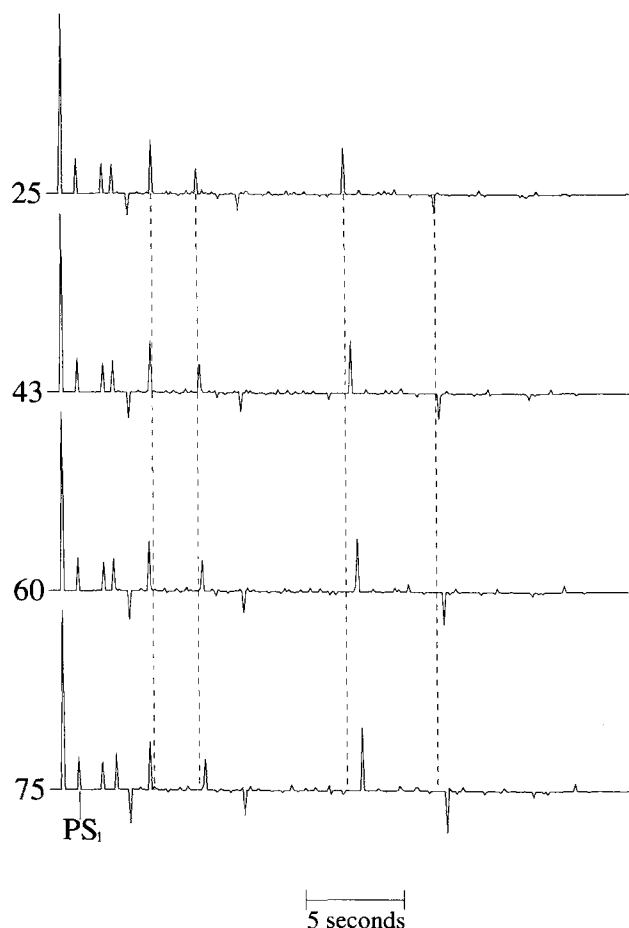


Figure 6. Synthetic receiver functions for a four-layer model for an impulse source observed at distances of 25°, 43°, 60° and 75°. The dashed vertical lines show how the arrival times of certain phases change with distance. For the velocity models in each layer, the values of P velocity (km s^{-1}), S velocity (km s^{-1}), density (g cm^{-3}), and thickness (km) are: first layer—5.1, 2.9, 2.5, 5.0; second layer—5.9, 3.4, 2.7, 10.0; third layer—6.7, 3.8, 2.9, 20.0; and fourth layer—8.1, 4.5, 3.3.

when we used a source function long enough to smear out the first two arrivals in Fig. 6, we obtained a shear velocity in the uppermost layer that was 15 per cent too large.

To evaluate the summations in eq. (7) to find the calculated radial-component signal, in principle one must consider all possible converted and transmitted rays in the crustal layer. However, in practice we need only include rays which arrive with significant energy. This ray set always includes the direct P ray, which is the reference for both traveltime and amplitude. In addition, for each boundary introduced into the crust (including the Moho), we add six rays (in Fig. 7 'c' represents two rays), thus, if the crust has n layers the number of rays is $(6n + 1)$. Usually there is little energy for rays which possess an S - P conversion at the free surface and a P - S conversion at the layer boundary, thus we include them only for boundaries with a strong velocity contrast. We will discuss this further in the next section.

Our present software calculates radial-component seismograms for crustal models with as many as five layers overlying a half-space. For each layer, the P velocity, S velocity, and layer thickness are free parameters, while we assume a density corresponding to the S velocity, as determined from the Nafe

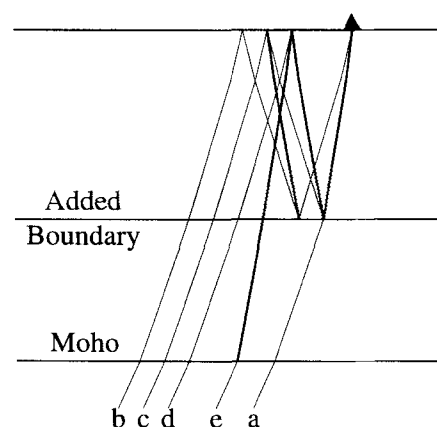


Figure 7. Rays added for each additional crustal boundary. Thicker lines represent S_v segments; thinner lines are P segments. Six rays are added for each additional boundary: a— PS (P converts to S_v at this boundary); b— PP_bP (subscript 'b' means ray reflected back from added boundary); c— PP_bS and PS_bP ; d— PS_bS ; e— SS_bS . In this notation, the first P of rays b, c, and d is the P ray from the Moho to the free surface; the first S in ray e is the P -to- S_v converted ray at the Moho, which travels to the free surface as S_v .

table (Ludwig, Nafe & Drake 1973). The scheme is fast: on a Sparc 10 machine, it takes 1 s to search about 200 four-layer models and fit seismograms with 800 points, or about 450 models of three-layer-over-half-space and fit seismograms of 300 points, which is long enough in practical use.

To determine the velocity structure beneath any particular station, we use a grid-search method to find the velocity model which provides the closest fit to either a single seismogram or a suite of seismograms if available for that station. It is impractical to perform the search over the entire possible range of crustal models, since we have too many free parameters (17 for a five-layer crust). Thus we first find the best-fitting layer-over-half-space model, then add boundaries to form more complex models. If we are fitting data from only one seismic event, the program requires only a few minutes to search all reasonable layer-over-half-space models.

TESTS ON SYNTHETIC WAVEFORMS

In this section, we perform a variety of tests to evaluate how the SORVEC algorithm responds when applied to synthetic data sets with various properties that are like those expected for real-world data. In particular, we consider three specific questions.

(1) To what extent is significant information lost because our algorithms generate synthetic waveforms by considering only a subset of all possible rays representing near-station crustal reverberations, i.e. only $(6n + 1)$ rays for an n -layer-over-a-half-space crustal model?

(2) How well does our algorithm perform if the teleseismic compressional-wave signal arriving at the base of the crust possesses considerable complexity, such as multiple subarrivals caused by reverberations produced by near-source crustal layering producing late arrivals having roughly the same ray parameter as the signal of interest?

(3) How well does the algorithm perform if the input signals are noisy, i.e. what are the maximum ambient noise levels for

which we still be able to use SORVEC to determine crustal structure?

Our approach to answering these questions is to use a complete Haskell matrix approach (Haskell 1962) to calculate synthetic vertical- and radial-component 'data' seismograms (e.g. see 'Z' and 'data' waveforms in Fig. 8) representing signals from a teleseismic source ($\Delta = 40^\circ$) recorded by a station overlying a layered crust. In these tests this crust is a three-layer-over-a-half-space Basin and Range model (Priestly & Brune 1978), with shear velocities of 2.05 km s^{-1} , 3.57 km s^{-1} , and 3.85 km s^{-1} within layers of thickness 2.5 km, 22.5 km, and 10 km, respectively, and P velocities related to the shear velocity using the relationship of Ludwig *et al.* (1973). Then, we use the SORVEC method described above to generate synthetic waveforms for a range of crustal models with shear velocities and thicknesses surrounding the values above; as we allow nine values for each of the six parameters, we consider 531 441 models. A graphical comparison of the misfit (e.g.

Fig. 8, right-hand side panels) between each of these synthetics and the Haskell-matrix-generated 'data' allows us to evaluate whether waveforms generated by the SORVEC method are sufficiently similar, and whether a grid-search inversion using SORVEC would be able to resolve the essential features of the crustal structure.

Effect of using $(6n + 1)$ rays

Intuitively, constructing a proper ray-theoretical seismogram for a station overlying a layered crust seems difficult, since there are an infinite number of rays produced by reflections and conversions within the various layers; however, usually only a rather small number of rays contribute significant energy to the waveform. In practice, it is sufficient and considerably more efficient to evaluate a finite subset of rays rather than perform a full Haskell matrix calculation. For example, Hron, Kanasewich & Alpaslan (1974) evaluated rays for a four-layer-over-a-half-space crustal model possessing a rather

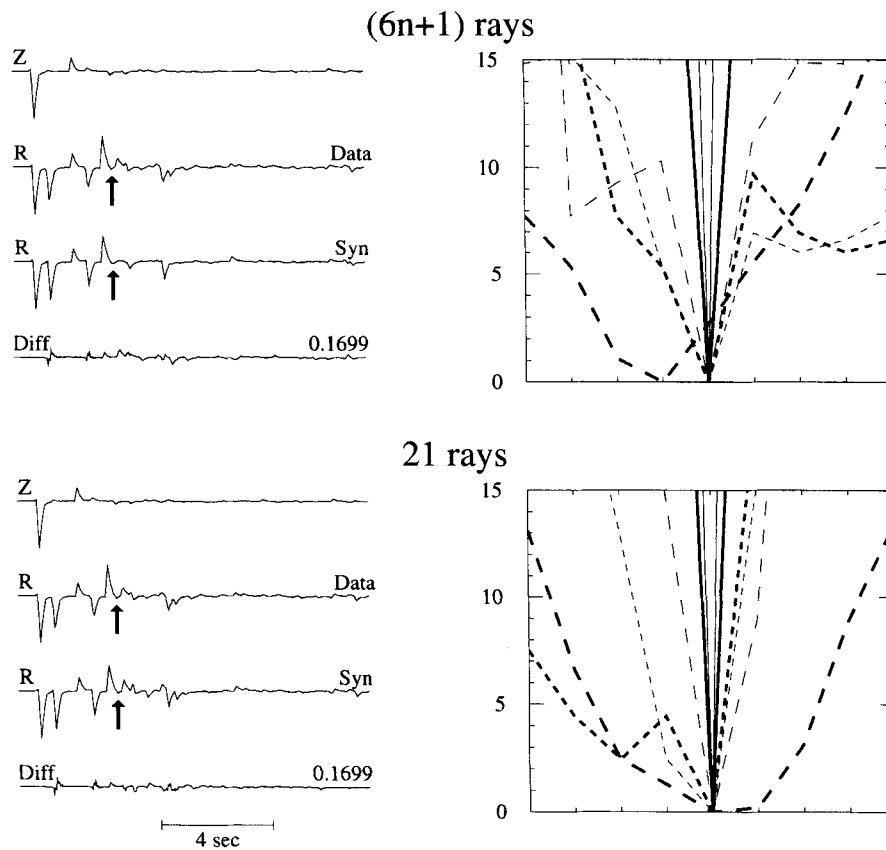


Figure 8. Comparison of synthetic waveforms generated by different methods when a teleseismic triangular source pulse interacts with a three-layer-over-a-half-space Basin and Range crustal model (see Priestly & Brune 1978). Here the 'Data' trace using a Haskell matrix method and two different sets of rays are used. The upper left panel shows waveforms generated using the $6n + 1$ rays (i.e. 19 rays) built into the SORVEC algorithm, as used for this paper; the lower left panel shows waveforms generated using 21 rays, i.e. all rays with amplitudes 5 per cent or more of the incident P wave. The two panels on the right-hand side show how well the waveforms constrain the layer thicknesses and shear velocities of the three layers: the horizontal axis is the range of permitted values for each of the six parameters (see below) and the vertical axis is the misfit increase (determined from eq. 10), plotted as a fraction of the minimum misfit. The graphed lines indicate the minimum value of the relative error obtained when each parameter is held fixed at the indicated value, and the other five parameters are allowed to vary over all possible values. The dark lines are misfits for the velocities and light lines are for layer thicknesses; solid lines are for the first layer; short dashed lines for the second, and long dashed lines for the third. The arrows highlight the portion of the waveform having the largest difference between raysets and synthetic data. 'Diff' is the difference between the data and synthetics; the number on the right is the maximum trace amplitude expressed as a fraction of the maximum data amplitude. The range of values plotted for shear velocities and layer thicknesses follow: 1st layer: $1.95\text{--}2.15 \text{ km s}^{-1}$, $1.5\text{--}3.5 \text{ km}$; 2nd layer: $3.37\text{--}3.77 \text{ km s}^{-1}$, $20.5\text{--}24.5 \text{ km}$; 3rd layer: $3.65\text{--}4.05 \text{ km s}^{-1}$, $6\text{--}14 \text{ km}$.

large 112 per cent shear velocity increase between the second and third layers, and concluded that only 21 rays had amplitudes of 5 per cent or more of the initial P ray, and only 99 rays had amplitudes exceeding 1 per cent. For most real-world applications, a synthetic waveform including all rays with amplitudes of 1 per cent or more would be excellent, and 5 per cent would be very adequate.

However, why limit the number of rays at all, since it now only takes us about 4 s on a Sparc 10 to generate the 'data' synthetics in Fig. 8 using a Haskell matrix approach with a time spacing of 0.025 s and 2048 frequency points? The answer is that 4 s is too time-consuming to be practical for many inversion problems; for example it would require almost a month of computing to sample the 531 441 crustal models to find the 'best' crustal model matching a particular data waveform (see Fig. 8). Haskell matrix methods are indeed appropriate for use with a small number of models (e.g. Owens *et al.* 1984), or when only lower-frequency information about waveforms is required, such as for synthesizing surface waves at regional distances.

In our SORVEC we add six rays for each additional layer. If the crust does not have a very strong reflector, the largest arrival after the direct P ray on the radial component is the P -to- S conversion at the Moho, with an amplitude of about 30 per cent of the P ray. However, for our test model, the Basin and Range model, there is a 74 per cent shear velocity increase between the first and second layers, thus after the P ray there is an arrival with an amplitude 80 per cent of P produced by a P -to- S conversion at the layer boundary. Rays propagating further after this ray can have large amplitudes; for example the amplitude of the S ray that reflects back from the free surface and returns to the first layer boundary is 23 per cent (see the arrows on the 'R' waveforms in Fig. 8). This ray is not one of the six included in our SORVEC algorithm, and it is clearly missing in the 'Syn' waveform in Fig. 8.

Nevertheless, the SORVEC algorithm is able to resolve the details of crustal structure; it correctly finds five of the six free crustal parameters, even though it uses only $(6n + 1)$ rays per layer (Fig. 8). For the sixth parameter, the shear velocity in the third layer, the SORVEC algorithm chooses 3.80 km s^{-1} , rather than 3.85 km s^{-1} , the proper value. There is only a slight improvement in resolution if we utilize a ray set including all 21 rays with amplitudes of 5 per cent of P or greater. However, while the grid search correctly finds all six model parameters, the shear velocity in the third layer is still poorly resolved, as indicated by the flat-bottomed portion of the trough in the misfit-versus-velocity graph in Fig. 8.

Generally, the $(6n + 1)$ rays utilized by SORVEC are adequate because, at teleseismic distances, the rays do not approach critical incidence, i.e. the reflection/transmission coefficients at layer boundaries are less than 1.0, usually less than 0.2, and rays steadily lose energy each time they interact with a boundary. This is unlike waveform modelling at regional distances, where trapped rays undergoing critical reflections may possess considerable energy (e.g. Zhao & Helmberger 1991, 1993). In Fig. 9 we illustrate the situation for a two-layer-over-a-half-space crust (the model of Fig. 4) and the family of rays having exactly one S path within the two crustal layers. Here, shear velocity contrast between the two layers is 19 per cent and the largest-amplitude ray not included in our $(6n + 1)$ set has an amplitude of 0.37 per cent of that of the P ray. Larger amplitudes generally occur only in exceptional

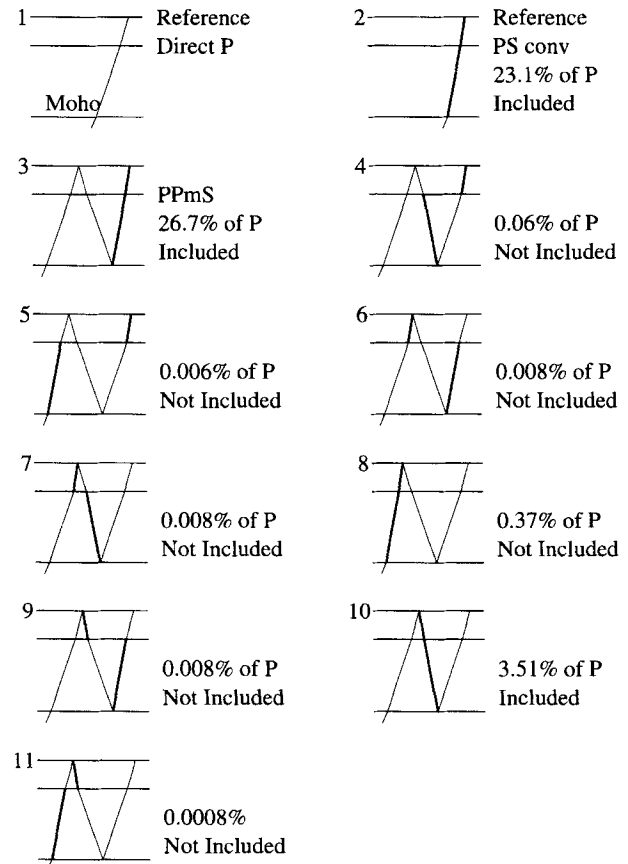


Figure 9. The relative importance of different rays. Dark lines are for S_s segments, light for P segments. 'x% of P ' means the amplitude is x per cent of the direct P ray, calculated for the same velocity model as in Fig. 4. 'Included' means the pictured ray is included in the $(6n + 1)$ ray set. Rays 3 to 11 in this figure include all rays having the same traveltime as ray 'g' in Fig. 4.

situations, when there are model boundaries with unusually high velocity contrasts at layer boundaries, such as the 74 per cent in the Basin and Range model. Even in these cases, the $(6n + 1)$ rays utilized by the SORVEC algorithm are sufficient for determining crustal structure (Fig. 8). While more rays will do a better job in theory, in practice real teleseismic data are always noisy and thus the missing rays do not contribute significantly.

Source signal complexity

For many real teleseismic waveforms, the signal leaving the near-source region has a complexity which might limit our ability to resolve near-station crustal structure. For example, for shallow earthquakes, crustal reverberations in the near-source region may produce arrivals following the initial P that strongly resemble reverberations originating in crustal layers near the receiving station (e.g. Fig. 10). For these waveforms the SORVEC grid search still returns the proper optimum values for the six crustal parameters (Fig. 10, right-hand-side panel). However, extra source complexity does smear out the resolution and cause significant uncertainty in the velocity and thickness of the lower two layers, as compared to the case in Fig. 8.

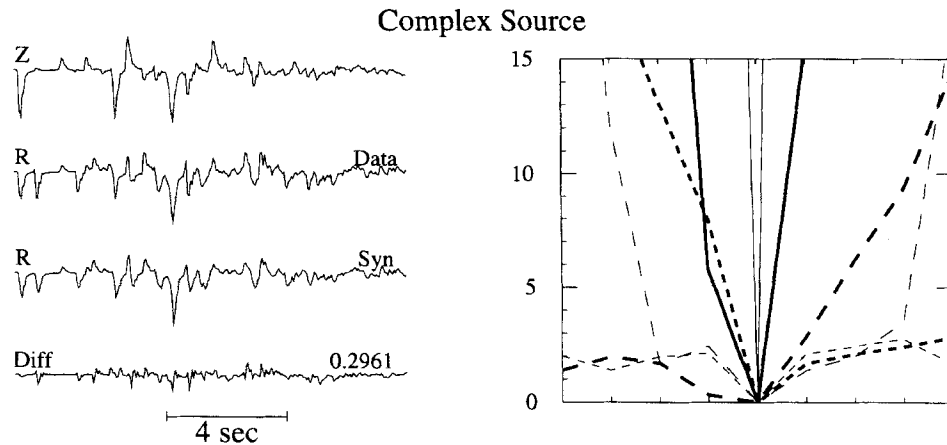


Figure 10. Synthetic waveforms generated by a complex teleseismic signal interacting with the Basin and Range crustal model. The complexity in the teleseismic signal stems from the crustal reverberations generated when an impulsive source is placed at a depth of 10 km within the crust. The remaining layout of the figure is as in Fig. 8, with the 'Syn' trace including only the $(6n + 1)$ rays which are utilized by our SORVEC algorithm.

Noisy waveforms

To evaluate the effect of noisy data on the SORVEC algorithm, we add various proportions of a computer-generated random noise signal to the vertical- and radial-component data (Fig. 11) and compare the fit between these data and the SORVEC-generated waveforms for each of the 531 441 crustal models. When the noise level is fixed at 10 per cent of the radial-component maximum, the thickness and shear velocity of the first layer are well-resolved. However, there is a trade-off between the velocities and thicknesses of the second and third layers; basically the grid search demonstrates that the velocity of the second layer cannot be smaller than 3.52 km s^{-1} , the velocity of the third layer cannot be greater than 3.95 km s^{-1} , and the thickness of the third layer cannot be smaller than 8 km. The resolution is slightly poorer for data with a 20 per cent noise level; however, the velocity and the thickness of the uppermost layer are still well resolved. When the noise level is 40 per cent none of the six parameters is well determined.

The situation improves considerably if we jointly evaluate a suite of noisy waveforms, synthesized to represent three earthquakes occurring at distances of 40° , 50° , and 60° from the receiver (Fig. 12). For a 20 per cent noise level the thickness and shear velocity of the first layer is well-determined and the thickness of the third layer is constrained to be 8 km or greater; five of the six parameters achieve their optimum fit at the appropriate value. Even when the noise level is 40 per cent the SORVEC algorithm is able to resolve the velocity and thickness of the uppermost layer (lower panel, Fig. 12), although the other layer parameters are still poorly determined.

APPLICATIONS

Station LZH

To illustrate the SORVEC method, we apply it to extract the crustal and uppermost mantle velocity structure for two digital stations in Tibet: LZH and AMDO. Station LZH is situated on the north-eastern boundary of Tibet (36.084°N , 103.834°E) in a complex region where we might expect the crustal thickness to be anywhere from 30 to 80 km. The only previous result is

from the P_n tomography study of Zhao & Xie (1993), who obtained a crustal thickness of $68 \pm 5 \text{ km}$ using P_n traveltime residuals and assumed that the regional crustal structure was similar to the TIP model (Zhao, Helmberger & Harkrider 1991), obtained from modelling Love waveforms from southern Tibet.

For the present study, we used waveforms from a deep-focus earthquake which occurred on 1992 January 20 at a distance of 31° from LZH in the Bonin Island region (ISC location: 27.93°N , 139.47°E , focal depth 512 km from pP - P times; m_b 5.8). Close inspection of the vertical- and radial-displacement waveforms (Fig. 13) indicates that the maximum of the radial-component signal occurs about 0.15 s later than the vertical-component signal. We interpret this as occurring as a result of the P - S_v converted phase at the uppermost crustal boundaries being more prominent in the radial-component signal. The difference of 0.15 s suggests the uppermost lowest-velocity crustal layer is quite thin. Differences in the vertical- and radial-component signals between 7–12 s are due to P - S_v conversion at the Moho ('a' in Fig. 13), P_s in B  th & Stef  nsson's (1966) notation. Another difference occurs at about 25 s (see 'c' in Fig. 13), which is $PpSmp$ and $PpPms$. The difference at about 32 s is the 'd' phase, which is $PpSms$. The ray paths for these phases are given under the same name in Fig. 3.

These differences provide sufficient information to allow us to constrain the crustal model beneath LZH. Using the SORVEC software, we determined the optimum solution for crustal models with a one-, two-, three-, and four-layer crust (Table 1 and Fig. 13). Note that the radial-component signal calculated for a one-layer crust ('syn1' in Fig. 13) does not produce good fit for the first arrival. The fit is much better for the signal calculated with a two-layer crust ('syn2' in Fig. 13); this implies that the uppermost crust beneath LZH possesses a layer with a thickness of about 1 km, with a shear velocity close to 2.0 km s^{-1} . As more layers are added, the fit improves for phases 'c' and 'd' at about 25 s and 32 s (Fig. 13). While a top layer of 2.1 km s^{-1} with a thickness of 1.2 km generates a good fit to the first arrival, that of 1.8 km s^{-1} with a thickness of 0.7 km generates a better fit to the later arrivals. For a four-layer crustal model, the error (eq. 10) is approximately 30 per cent less than for a one-layer model.

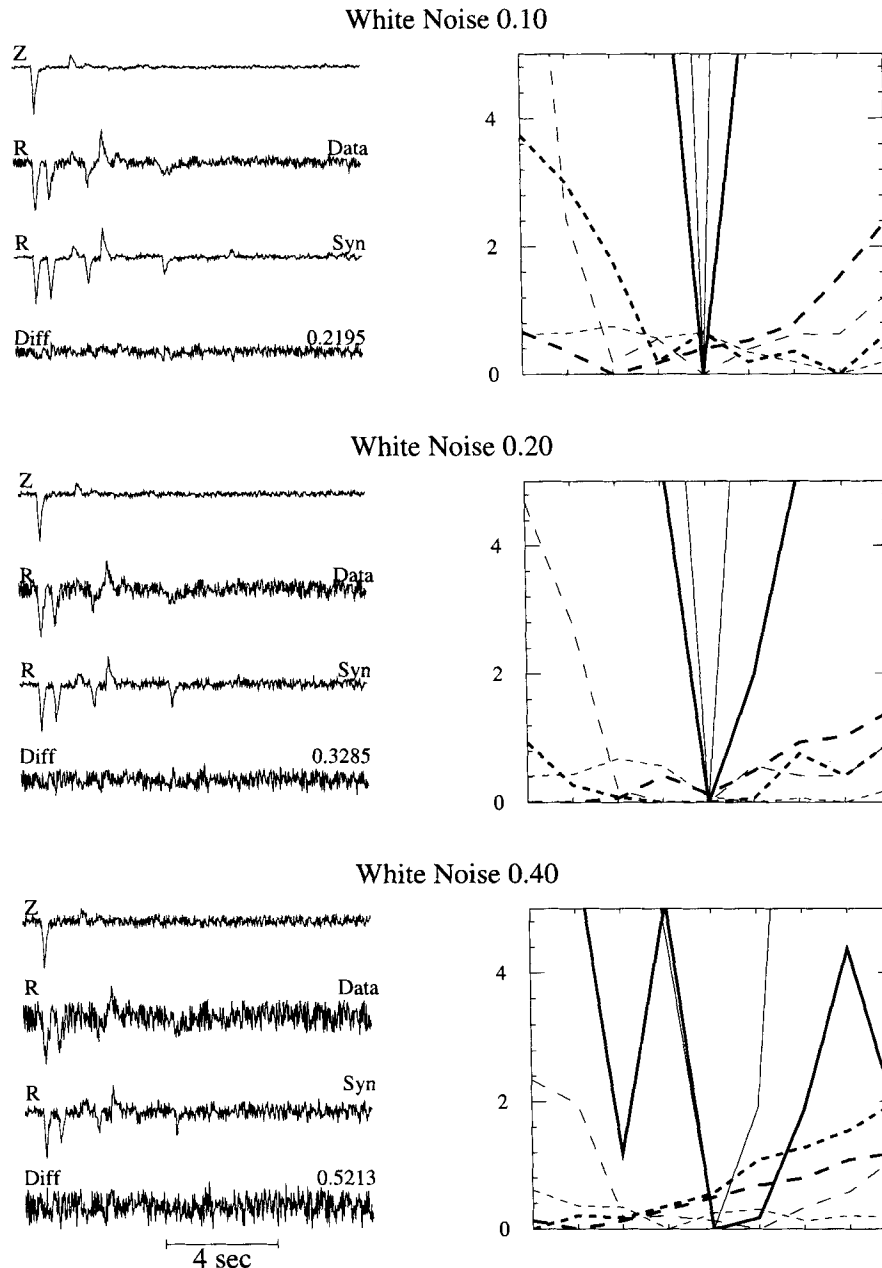


Figure 11. Synthetic waveforms analysed and presented as in Fig. 8, except with various proportions of random noise added to both the vertical- and radial-component waveforms. The noise signal is formed by generating random numbers uniformly over the interval $(-1, +1)$, combined with the waveforms so that the maximum noise signal added is 10 per cent (top), 20 per cent (centre), and 40 per cent (bottom) of the maximum amplitude of the radial-component signal. Vertical-component signals appear less noisy than radial-component signals because maximum vertical-component amplitudes are greater.

The crustal thickness is about 6.5 km, and shear velocity in the mantle is about 4.4 km s^{-1} . This agrees well with the result of Zhao & Xie (1993), determined using P_n tomography, even though the crustal velocity structure we obtain is generally much slower than that of TIP model (Zhao *et al.* 1991), which they assumed.

If the crustal model has more than a few layers, it is almost impossible to perform a grid search over all reasonable crustal models. However, a thorough search is easy for a five-parameter layer-over-half-space model, and this illustrates some important general features about how the fit to the data depends on the model parameters (Fig. 14). For example, note

that most of the graphed lines in Fig. 14 are not smooth, possessing many local minimums. This implies that linearized inversion methods will be ineffective at finding the global, optimal solution. Because the graphed lines show that relative error varies significantly over the range of reasonable values, Fig. 14 also illustrates that the data place relatively strong constraints on the crustal P velocity, the crustal S velocity, and the crustal thickness.

However, it is also clear from Fig. 14 that the mantle S velocity is not very well constrained, and mantle P velocity is not constrained at all. Indeed, Fig. 15 demonstrates that variations in the mantle P velocity have almost no effect on the

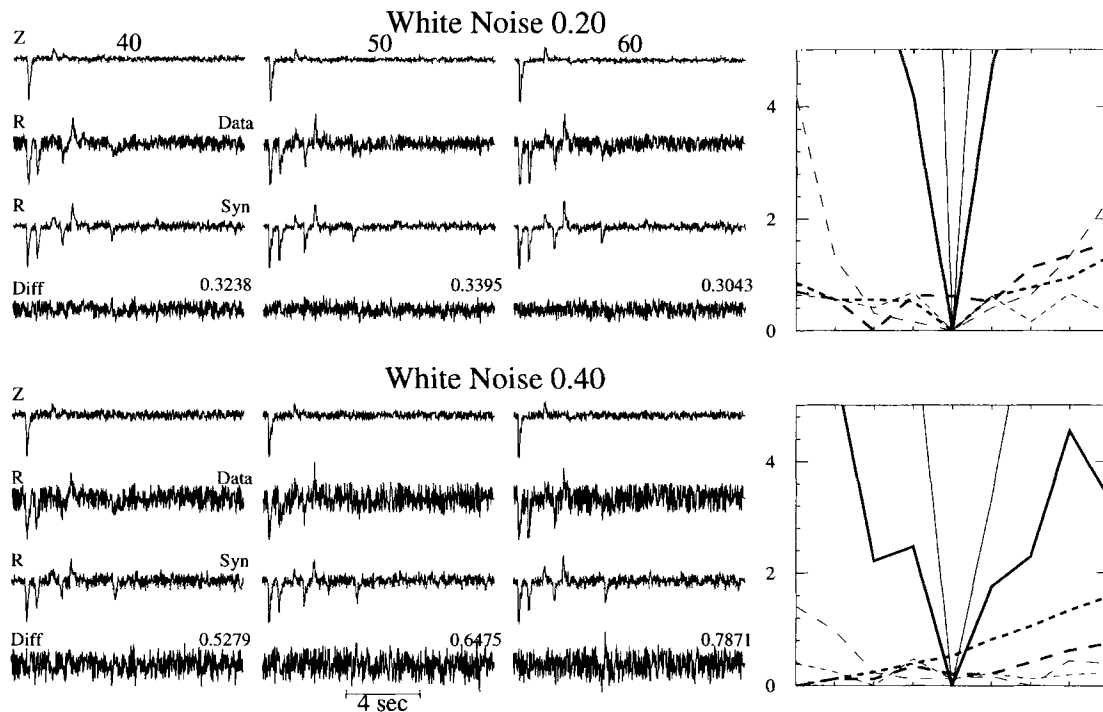


Figure 12. Noisy synthetic waveforms analysed and presented as in Fig. 11, except that the SORVEC algorithm combines information from stations at three distances (40°, 50° and 60°) to evaluate how well the data constrain the shear velocities and layer thicknesses of the crustal model. The figure presents trials for noise levels of 20 per cent (top) and 40 per cent (bottom) of the maximum radial-component signal.

Table 1. Models for station LZH.

	syn1			syn2			syn3			syn4		
	α	β	Th	α	β	Th	α	β	Th	α	β	Th
Crust	6.60	4.10	56.0	6.40	3.77	49.2	5.62	3.37	44.4	5.30	3.17	26.0
										5.70	3.39	16.8
Mantle	7.50	4.90		7.90	4.40		6.90	4.02	19.9	6.90	4.02	19.9
							7.90	4.40		7.80	4.43	

α is compressional velocity, β shear velocity, in km s^{-1} . Th is layer thickness in km.

expected amplitude of the most important rays ('a' to 'e' in Fig. 3, 'b' ray is missing, since its contribution is of second order) contributing to the radial-component signal. This implies that we need not vary the mantle P velocity when we search for the best-fitting two-layer or many-layer crustal models; rather, we can choose a P velocity that fits the Nafe table for a given mantle S velocity. One reason that mantle P velocities are so poorly constrained is that there is a relatively small range of 'reasonable' values: $7.5\text{--}8.5 \text{ km s}^{-1}$ represents a velocity change of less than 15 per cent. This means that the possible range of reflection and transmission coefficients is also small, since these are constrained by the relative amplitudes of converted phases and the direct P phase. This is an inherent limitation of all methods which attempt to recover receiver structure from teleseismic P waveforms. Neither the SORVEC method nor any other receiver function method utilizing teleseismic P waveforms will place strong constraints on mantle P velocity.

Station AMDO

Station AMDO was a temporary seismic station operating in Tibet (32.247°N , 91.688°E) between 1991 July 1 and 1992

June 30 (Owens *et al.* 1993). Little is known about the crustal structure near AMDO; however, Zhu *et al.* (1993) evaluated receiver functions at some nearby stations. The P_n traveltime tomography analysis of Zhao & Xie (1993) suggests that the crustal thickness is somewhere between 70 and 80 km, and the P_n velocity is about 7.9 km s^{-1} . The crustal thickness was obtained by assuming a crustal TIP model (Zhao *et al.* 1991).

In the present study, we apply the SORVEC procedure to long-period waveforms obtained by filtering the recorded broad-band waveforms with long-period Press–Ewing instrument response (first two traces in each group, Fig. 16). The broad-band data are recorded at AMDO from 13 different earthquakes (Table 2). We have selected these events to represent the best available waveforms from a broad range of azimuths surrounding AMDO; this allows us to investigate whether the optimal crustal structure depends on signal azimuth. The data is of variable quality, because, in some azimuthal directions, there is only one event available (e.g. note waveforms from back azimuths of 181° and 295° in Fig. 16); however, most of the waveforms are of good quality.

We first apply the SORVEC procedure to determine the four-layer crustal model (see model labelled 'All' in Table 3)

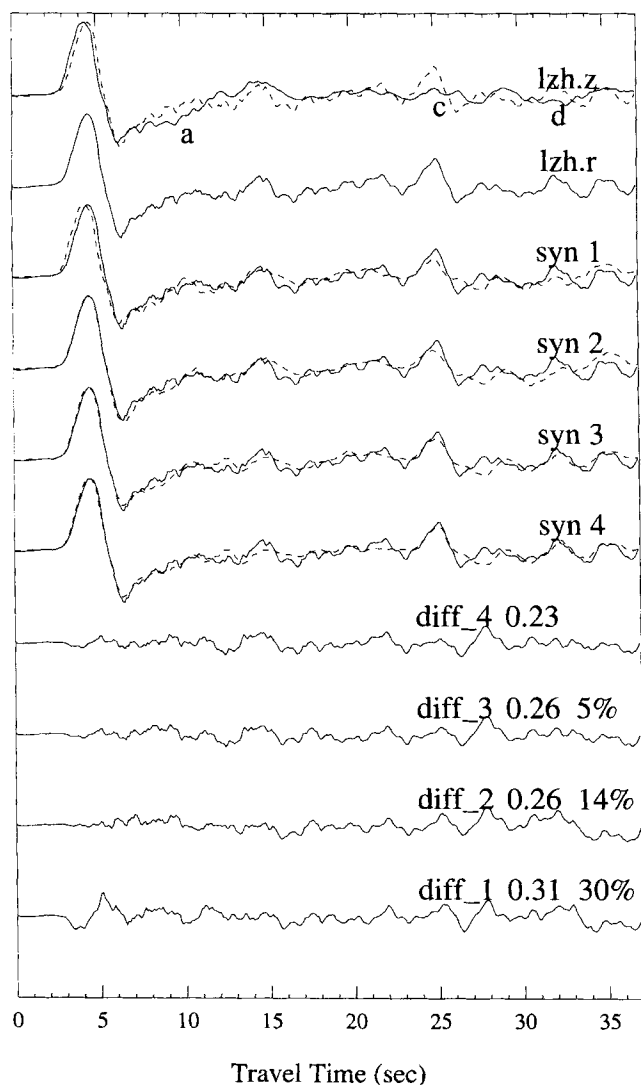


Figure 13. Vertical- and radial-component signals (solid lines labelled 'lzh.z' and 'lzh.r') from the Chinese station LZH, and radial-component synthetics generated using the SORVEC method for four different crustal models (dashed lines labelled 'syn 1', etc.; see Table 1). For ease of comparison, the radial-component signal at LZH is plotted as a dashed line with the top trace, and as a solid line with syn1, syn2, etc. The traces labelled 'diff 1', etc. are the differences between the observations and the synthetics; the two numbers on the right are the maximum difference, expressed as a fraction of the maximum of the 'lzh.r' trace, and the relative error, i.e. the error increase compared with the minimum error of syn4.

that provides the optimal fit to the entire suite of 13 waveforms (Table 2 and Fig. 16). If we measure fit by evaluating the ratio of the maximum of the difference signal to the synthetic signal, fits for six of the 13 waveforms are good, having a difference of 0.4 or less. Fits are poor for four waveforms, as the difference ratio is 0.6 or greater. We attribute these poor fits to the noise level of the recorded waveform. For example, the earthquake at back azimuth 181° had a magnitude of only 5.4; inspection of the signal prior to the initial arrival suggests that the noise level is at least one-quarter of the maximum amplitude.

The optimal crustal model we obtain has a crustal thickness of 75 km (model 'All' in Table 3), overlying a mantle with a shear velocity of 4.40 km s^{-1} . The third layer has a distinctly

lower shear velocity (3.55 km s^{-1}) than the second layer (3.80 km s^{-1}), possibly indicating partial melting within the lower crust. As discussed above (Fig. 15), the mantle P velocity of 7.9 km s^{-1} is not meaningful, as it is determined from Nafe's table from the mantle shear velocity of 4.40 km s^{-1} .

To investigate whether a single crustal model is appropriate for signals arriving from different directions, we determined individual models (Table 3) for six waveforms with an azimuthal spacing of about 40° . Generally the fits for these individual models (Fig. 17) are only somewhat better than that for the 'All' model. The fits for the waveforms at back azimuths of 181° and 295° are still not very good (difference ratios of 0.74 and 0.55), although the improvement over model 'All' is significant. The overall fit for the individual model at 181° is especially poor, even though the fit is improved for the first 20 s of the signal. Note that the single model predicts a very good fit to 295° data.

A comparison of the individual models and model 'All' shows that they are reasonably consistent with one another. All have a crustal thickness of between 70 and 80 km, except model 295° , with a thickness of 60 km. All have a low-velocity layer in the lower crust, except model 181° . The waveforms at 181° and 295° are both noisy (Fig. 17), and both occur at azimuths where we have few events for comparison. The fit to the data at 295° is acceptable, but the fit at 181° is not. Generally, model 'All' appears to provide a reasonable, representative model of the crust beneath station AMDO for signals from a variety of azimuths. This result agrees well with the previous study of Zhao & Xie (1993).

DISCUSSION AND CONCLUSIONS

In this paper we have developed a new and practical modification of the receiver-function approach, the SORVEC method, which can be used to determine near-station crustal structure from teleseismic body-waveforms arriving 30–50 s after the first P arrival. These signals can be used to investigate crustal structure because the most energetic features within them are caused by internal reflections and conversions within crustal layers. For the SORVEC method, we have developed a formula describing the radial-component signal in terms of an assumed crustal structure, and a second-order expansion of the vertical-component signal in terms of rays representing reverberation within the crust. Then, using this formula, we have varied the crustal structure to obtain an optimum fit between observed and synthetic radial-component signals. To apply the method we have made no additional assumptions, except to limit the number of rays used in the synthetic procedure.

We have written a FORTRAN program implementing the SORVEC method, and testing with synthetic data has demonstrated that the method is effective for recovering crustal structure, in spite of the second-order approximations or the limited number of rays. As a practical test, we have applied the method to determine crustal structure beneath stations LZH and AMDO in Tibet. At LZH, the crustal thickness is 65 km; beneath station AMDO, the crustal thickness is about 75 km, and there is a distinct low-velocity layer occurring at a depth of about 25–35 km.

What are the advantages and disadvantages of using the SORVEC method? One important advantage arises because it is computationally very fast, and it is thus a practical basis for grid-search methods. We suggest that SORVEC is the method

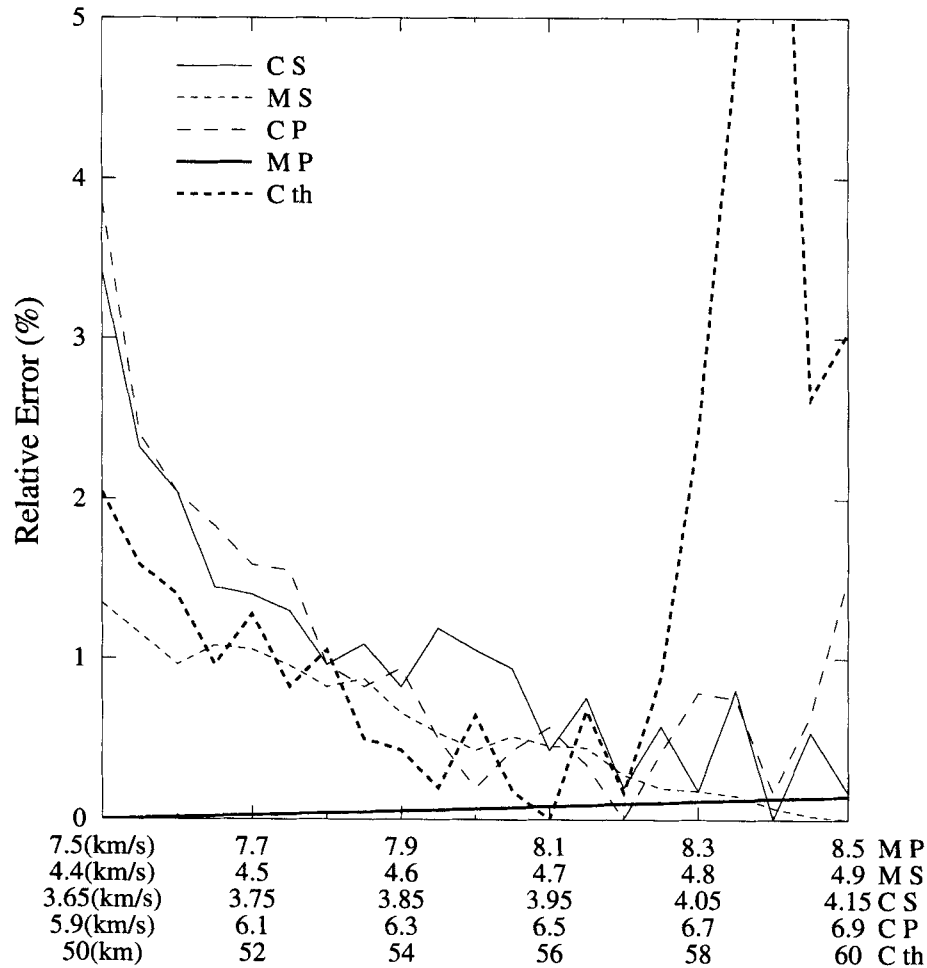


Figure 14. Effect of variation of model parameters for model 'syn 1' on fit to trace 'lzh.r' at station LZH. Relative error is the difference between the misfit and the global minimum misfit, divided by the global minimum misfit. Model parameters are: 'CS'—crustal S velocity; 'CP'—crustal P velocity; 'MS'—mantle S velocity; 'MP'—mantle P velocity; and 'Cth'—crustal thickness. The horizontal axis gives the range of each of these parameters. The graphed lines indicate the minimum value of the relative error obtained when each parameter is held fixed at the indicated value, and the other four parameters are allowed to vary over all possible values.

Table 2. Events used for station AMDO.

ID	yr	mmdd	hhmm	sec	Location		Depth	Mb	Δ	B Az
					(°N, °E)		(km)		(°)	(°)
202	91	0721	2259	09.6	3.008	128.434	34	5.9	45.1	122
218	91	0806	1449	30.5	35.725	141.044	29	5.9	40.7	71
275	91	1002	1432	55.1	-10.402	161.363	91	5.4	50.6	181
311	91	1107	0921	23.7	-7.320	128.550	140	5.9	52.7	132
351	91	1217	0638	17.3	47.393	151.499	157	5.8	47.2	53
020	92	0120	1337	03.0	27.983	139.405	499	5.8	41.2	83
073	92	0313	1718	39.9	39.710	39.605	27	6.2	42.3	295
086	92	0326	1414	11.9	51.222	-179.723	33	5.9	64.8	44
094	92	0403	0319	51.4	-5.696	151.164	27	5.8	67.9	112
109	92	0418	0916	52.8	-5.454	103.001	29	5.7	39.0	162
110	92	0419	1832	19.0	23.861	121.594	16	5.8	27.6	100
128	92	0507	0623	36.1	41.175	144.700	13	5.8	42.9	62
142	92	0521	1805	52.5	-8.748	117.604	143	5.7	47.7	144

mmdd is month and day, hhmm is hour and minute, Δ distance. B Az is back azimuth. The location is from NEIC.

Table 3. Optimal models for station AMDO.

Event	B Az	Layer 1 α , β , Th			Layer 2 α , β , Th			Layer 3 α , β , Th			Layer 4 α , β , Th			Mantle α , β	
All		3.3	1.80	1.2	6.5	3.80	31	6.5	3.55	30	6.8	3.95	13	7.9	4.40
086	44	3.6	2.00	2.0	6.3	3.70	38	5.7	3.40	23	7.4	4.05	13	7.8	4.35
020	83	3.7	1.98	1.3	6.1	3.55	25	5.4	3.10	38	6.5	3.55	15	8.0	4.45
202	122	3.5	2.02	1.5	6.5	3.75	22	5.6	3.35	28	6.4	3.60	19	7.9	4.40
109	162	3.6	2.07	2.0	6.0	3.50	31	5.5	3.20	22	6.2	3.50	22	7.9	4.40
275	181	3.6	1.80	0.8	5.4	3.22	23	7.1	3.89	31	6.2	3.57	15	7.9	4.40
073	295	5.3	2.93	0.7	6.3	3.70	15	5.2	2.85	19	7.3	4.05	25	8.8	4.83

α is P velocity in km s^{-1} ; β is S velocity in km s^{-1} . B Az is back azimuth in degrees. Th is the layer thickness in km.

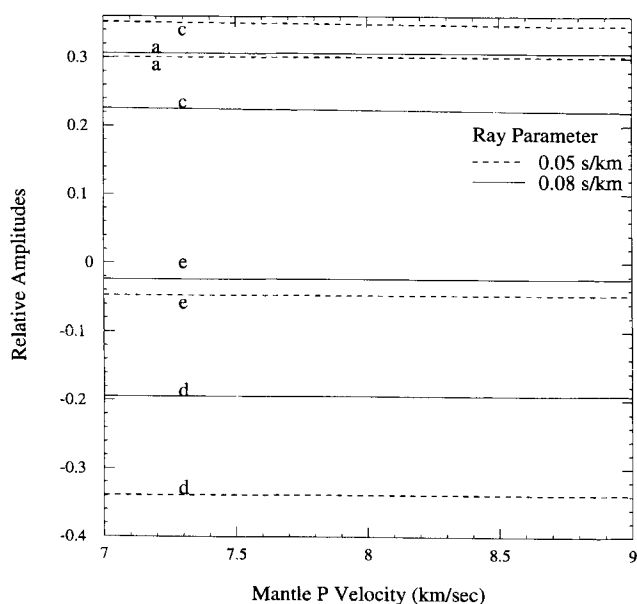


Figure 15. The dependence of relative amplitudes on variations in mantle P velocity for the four most important rays ('a' to 'e' in Fig. 3) contributing to the calculated radial-component signal at station LZH. The calculated amplitudes are for a layer-over-half-space model, as in Fig. 5. Solid and dashed lines are for ray parameters of 0.08 and 0.05 s km^{-1} , respectively.

of choice whenever there is reason to model the crust as consisting of a relatively small number (say four or fewer) flat-lying, constant-velocity layers. Alternatively, other, more computationally expensive, approaches are preferable in pathological situations where some of the layers have strong velocity gradients or significant dip angles, if there is considerable lateral heterogeneity, or if one prefers models with a large number (say twenty) of thin layers.

Another advantage of SORVEC is that it is applied to data waveforms in the time domain. While we lose some information because the method considers only a subset of all possible rays within the crust, the uncertainty caused by the phases that we ignore is probably no greater than that produced by deconvolution noise in frequency-based receiver-function methods. Although we have shown here how a complex source signal or the presence of noise can degrade the performance of our algorithm, this is true for frequency-based methods as well.

Any researcher considering how best to determine crustal structure should be aware of several problems which afflict all receiver-function methods. For example, there is an inherent

uncertainty in the crustal structure determined using receiver-function methods. Phase amplitudes are determined by the reflection/transmission coefficients at layer boundaries, which are a function of velocity ratios at the boundary, and the traveltime differences for individual crusts depend on the ratio of layer thickness and velocity. Since both depend on ratios of model parameters, it is difficult to distinguish two crustal models whose velocities and layer thicknesses are in direct proportion. Thus, in Fig. 18 and Table 4, synthetics generated for two models are almost identical because the two models have thicknesses and velocities differing by a roughly fixed proportion (3 per cent). We obtained model mdl2 by fixing the shear velocity for the uppermost crustal layer at 3.2 km s^{-1} , instead of 3.3 km s^{-1} as in mdl1.

Another issue is if it is appropriate to stack waveform data: if this is properly done, the signal can be greatly enhanced because this procedure can remove non-coherent signals; however, if the data are from several different azimuths and distances, for some crustal reverberations relative traveltime differences are large enough to significantly broaden a stacked signal (Fig. 6). Moreover, the amplitudes vary significantly as the ray parameter changes (see traces 'c' and 'd' in Fig. 15), further limiting the quantitative significance of stacked amplitudes. It is also inappropriate to use data from distance ranges in which many phases come in at roughly the same time, since those phases may have very different ray parameters. This includes data from distances of less than 25° , where the upper mantle triplication occurs, and data from the distance range of 75° – 90° , where PcP and P arrive at about the same time, but with different ray parameters.

As we have discussed previously, the receiver-structure problem is highly non-linear, thus there is no certainty that one will find a better solution than the initial starting model. The determination of many-layer crustal models using a grid-search method is often impractical, for while the method itself will always find the global optimum model, the process of performing the search may be prohibitively time-consuming. It is, however, considerably more efficient than Haskell matrix methods. However, with SORVEC methods it is possible to perform a comprehensive search for all reasonable models

Table 4. Sensitivity.

	mdl1			mdl2		
	α	β	Th	α	β	Th
Crust	5.80	3.30	15.0	5.63	3.20	14.6
	6.70	3.80	20.0	6.51	3.67	19.2
Mantle	8.30	4.60		8.05	4.46	

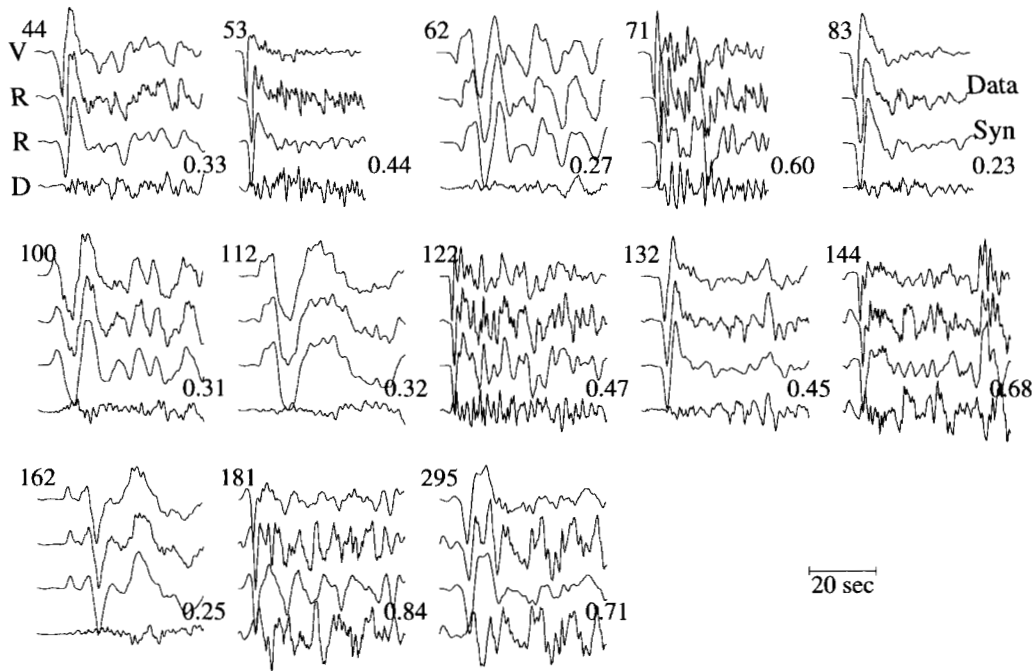


Figure 16. Vertical- and radial-component signals recorded at AMDO for 13 earthquakes (see Table 2), along with synthetic radial-component signals calculated for optimal model 'All' of Table 3. The 'difference' signal is the difference between the observed and calculated radial-component signals; the number on the right is the ratio of the maximum amplitudes of the difference and synthetic signals. The numbers on the left are the back azimuths (see Table 2). All plotted waveforms have been filtered to resemble data with a Press-Ewing instrument response.

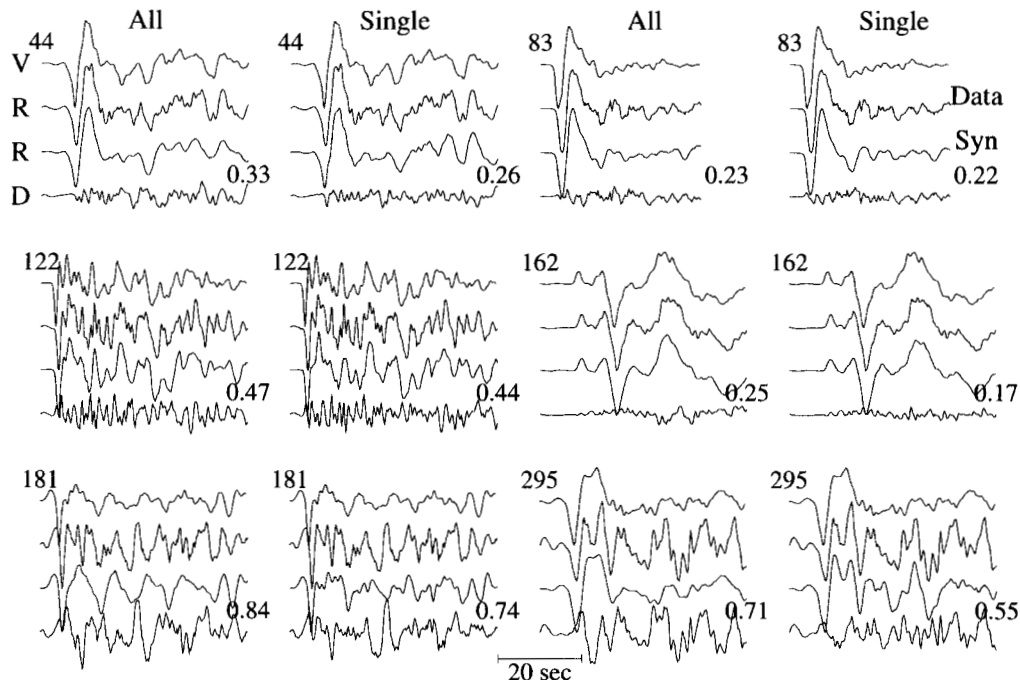


Figure 17. Comparison of data and radial-component synthetics for model 'All' with synthetics calculated for models fitted to six individual waveforms (Table 3). As in Fig. 16, numbers on the right are ratios of maximum amplitudes of difference and synthetic signals; numbers on the left are station-event back azimuths.

having a one-to-three-layer crust; these results provide a guide for the many-layer crust search, minimizing the chance that the inversion process will become trapped in a local minimum, or spend too much time investigating unrealistic crustal models.

ACKNOWLEDGMENTS

We would like to thank Dr Charles A. Langston, Dr Alan E. Beck, the editor, and an anonymous reviewer for their constructive suggestions and comments. All the data used are

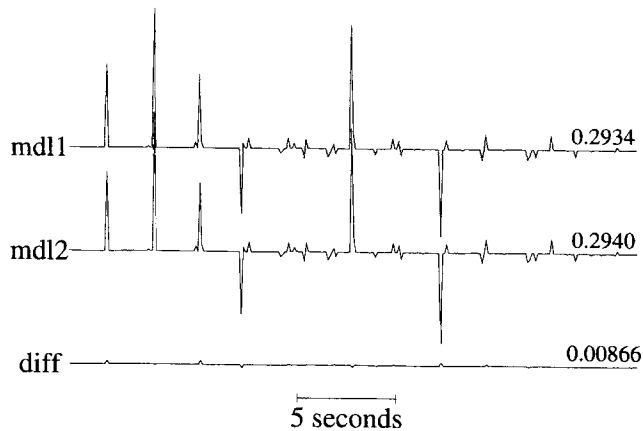


Figure 18. Receiver functions are nearly identical for two models (mdl1 and mdl2 in Table 4) whose velocities and layer thicknesses differ by roughly the same fraction (about 3 per cent). We plot only the arrivals following the direct *P* arrival, which is assumed to have a maximum amplitude of 1.0 in each case.

from IRIS data centre; help from Tim Ahern, Rick Benson, Taoul Titus and Glynis Wilson is appreciated. Partial support for this research was provided by the Air Force Office of Scientific Research under contract F49620-94-0287. Contribution number of 1152 of the Institute for Geophysics, the University of Texas at Austin.

REFERENCES

- Ammon, C.J., 1991. The isolation of receiver effects from teleseismic *P* waveforms, *Bull. seism. Soc. Am.*, **81**, 2504–2510.
- Ammon, C.J., Randall, G.E. & Zandt, G., 1990. On the nonuniqueness of receiver function inversion, *J. geophys. Res.*, **95**, 15 303–15 318.
- Båth, M., 1974. *Spectral Analysis in Geophysics*, Elsevier Scientific Publishing Company, New York, NY.
- Båth, M. & Stefánsson, 1966. *S-P* conversion at the base of the crust, *Ann Geofis.*, **19**, 119–130.
- Burdick, L.J. & Langston, C.A., 1977. Modeling crustal structure through the use of converted phases in teleseismic body-wave forms, *Bull. seism. Soc. Am.*, **67**, 677–691.
- Cassidy, J.F., 1992. Numerical experiments in broadband receiver function analysis, *Bull. seism. Soc. Am.*, **82**, 1453–1474.
- Dziewonski, A.M. & Anderson, D.L., 1980. Preliminary reference Earth model, *Phys. Earth planet. Inter.*, **25**, 297–356.
- Fuchs, K. & Müller, G., 1976. Comparison of synthetic seismograms with the reflectivity method and comparison of observations, *Geophys. J. R. astr. Soc.*, **23**, 417–433.
- Gurrola, H. & Minster, J.B., 1993. Resolution of velocity structure determined by velocity spectrum stacking of receiver functions, *Proc. 15th Annual Seism. Res. Symp.*, 125–131.
- Haskell, N.A., 1962. Crustal reflection of plane *P* and *SV* waves, *J. geophys. Res.*, **67**, 4751–4767.
- Helmberger, D.V., 1968. The crust–mantle transition in the Bering Sea, *Bull. seism. Soc. Am.*, **58**, 179–214.
- Helmberger, D.V., 1980. Theory and applications of synthetic seismograms, in *Proc. Int. Sch. Phys. 'Enrico Fermi', Course LXXXV, Earthquakes: Observation and Interpretation*, pp. 174–222, eds Kanamori, H. & Boschi, E., North-Holland.
- Hron, F., Kanasewich, E.R. & Alpaslan, T., 1974. Partial ray expansion required to suitably approximate the exact wave solution, *Geophys. J. R. astr. Soc.*, **36**, 607–625.
- Langston, C.A., 1977. The effect of planar dipping structure on source and receiver responses for constant ray parameter, *Bull. seism. Soc. Am.*, **67**, 1029–1050.
- Langston, C.A., 1979. Structure under Mount Rainier, Washington, inferred from teleseismic body waves, *J. geophys. Res.*, **84**, 4749–4762.
- Langston, C.A., 1989. Scattering of teleseismic body waves under Pasadena, California, *J. geophys. Res.*, **94**, 1935–1951.
- Ludwig, W.J., Nafe, J.E. & Drake, C.L., (1973). Seismic refraction, in *The Sea*, Vol. 4, Pt. I, pp. 53–84, ed. Maxwell, A.E., Wiley-Interscience, New York, NY.
- Mangino, S. & Ebel, J., 1992. The receiver structure beneath the Chinese digital seismograph station network (CDSN) stations: Preliminary results, *Phillips Lab. Tech. Rept. PL-TR-92-2149*.
- Owens, T.J., Zandt, G. & Taylor, S.R., 1984. Seismic evidence for an ancient rift beneath the Cumberland Plateau, Tennessee: A detailed analysis of broadband teleseismic *P* waveforms, *J. geophys. Res.*, **89**, 7783–7795.
- Owens, T.J., Crosson, R.S. & Hendrickson, M.A., 1988. Constraints on the subduction geometry beneath western Washington from broadband teleseismic waveform modeling, *Bull. seism. Soc. Am.*, **78**, 1319–1334.
- Owens, T.J., Randal, G.E., Wu, F.T. & Zheng, R., 1993. PASSCAL instrument performance during the Tibetan Plateau passive seismic experiment, *Bull. seism. Soc. Am.*, **83**, 1959–1970.
- Phinney, R.A., 1964. Structure of the Earth's crust from spectral behaviour of long-period body waves, *J. geophys. Res.*, **69**, 2997–3017.
- Priestley, K. & Brune, J., 1978. Surface waves and the structure of the great basin of Nevada and western Utah, *J. geophys. Res.*, **83**, 2265–2272.
- Zhao, L.-S. & Helmberger, D.V., 1991. Broadband modelling along a regional shield path, Harvard recording of the Saguenay earthquake, *Geophys. J. Int.*, **105**, 301–312.
- Zhao, L.-S. & Helmberger, D.V., 1993. Source retrieval from broadband regional seismograms: Hindu Kush region, *Phys. Earth planet. Inter.*, **78**, 69–95.
- Zhao, L.-S. & Xie, J., 1993. Lateral variations of the compressional velocity structure beneath the Tibetan Plateau from *P_n* travel time inversion, *Geophys. J. Int.*, **115**, 1070–1084.
- Zhao, L.-S., Helmberger, D.V. & Harkrider, D.G., 1991. Shear-velocity structure of the crust and upper mantle beneath the Tibetan Plateau and Southeastern China, *Geophys. J. Int.*, **105**, 713–730.
- Zhu, L.P., Zeng, R., Wu, F.T., Owens, T.J. & Randall, G.E., 1993. Preliminary study of crust–upper mantle structure of the Tibetan Plateau by using broadband teleseismic body waveforms, *Acta Seism. Sinica*, **6**, 305–316.